


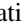
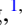

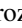





Electrical detection of the spin reorientation transition in antiferromagnetic TmFeO₃ thin films by spin Hall magnetoresistance

S. Becker ^{1,*}, A. Ross ^{1,2}, R. Lebrun ^{1,3}, L. Baldrati ¹, S. Ding ^{1,2,4}, F. Schreiber ¹, F. Maccherozzi ⁵,
D. Backes ⁵, M. Kläui ^{1,2,6} and G. Jakob ^{1,2}

¹*Institute of Physics, University of Mainz, Staudingerweg 7, 55128 Mainz, Germany*

²*Graduate School of Excellence “Materials Science in Mainz” (MAINZ), Staudingerweg 9, 55128 Mainz, Germany*

³*Unité Mixte de Physique CNRS, Thales, University Paris-Sud, Université Paris-Saclay, Palaiseau 91767, France*

⁴*State Key Laboratory for Mesoscopic Physics, School of Physics, Peking University, Beijing 100871, China*

⁵*Diamond Light Source, Harwell Science and Innovation Campus, Didcot OX11 0DE, United Kingdom*

⁶*Center for Quantum Spintronics, Norwegian University of Science and Technology, 7491 Trondheim, Norway*



(Received 16 October 2020; revised 16 December 2020; accepted 16 December 2020; published 14 January 2021)

TmFeO₃ (TFO) is a canted antiferromagnet that undergoes a spin reorientation transition (SRT) with temperature between 82 and 94 K in single crystals. In this temperature region, the Néel vector continuously rotates from the crystallographic *c* axis (below 82 K) to the *a* axis (above 94 K). The SRT allows for a temperature control of distinct antiferromagnetic states without the need for a magnetic field, making it apt for applications working at terahertz frequencies. For device applications, thin films of TFO are required as well as an electrical technique for read-out of the magnetic state. Here, we demonstrate that orthorhombic TFO thin films can be grown by pulsed laser deposition and the detection of the SRT in TFO thin films can be accessed by making use of the all-electrical spin Hall magnetoresistance, in good agreement for the temperature range where the SRT occurs in bulk crystals. Our results demonstrate that one can electrically detect the SRT in insulators.

DOI: [10.1103/PhysRevB.103.024423](https://doi.org/10.1103/PhysRevB.103.024423)

I. INTRODUCTION

Antiferromagnets (AFMs) are a key focus of current spintronic research [1–3]. Due to their fast spin dynamics and stability against external perturbations, AFMs are promising candidates for terahertz emitters [4,5] and next-generation data storage devices [6]. The insulating canted antiferromagnet TmFeO₃ (TFO) has recently gathered significant interest because of the possibility to coherently switch its spin state by 90° with a terahertz pulse [7] in the proximity of the temperature-driven spin reorientation transition (SRT) in bulk single crystals. The detection of the switching was achieved by the Faraday effect in a transmission geometry. However, not only are bulk crystals inappropriate for back-end integration into devices, but also the requirements of writing and read-out by terahertz laser pulses necessitate large external power sources. Moving towards applications, then, requires high-quality thin films possessing similar antiferromagnetic properties to their bulk counterparts and integrated mechanisms for controlling and reading the antiferromagnetic Néel vector. The growth of different antiferromagnetic thin films can be achieved via several techniques including sputtering [8] and pulsed laser deposition [9]. Meanwhile, current-induced control of the Néel vector has recently been shown in antiferromagnetic insulators [10], while the electrical readout has been achieved making use of the spin Hall magnetoresistance (SMR) between a heavy metal and an antiferromagnetic insulator [10,11]. With respect to TFO thin films, growth has

been achieved in the hexagonal phase when deposited on Al₂O₃ (0001), Pt (111) [12,13], and yttria-stabilized zirconia (YSZ) (111) [14] substrates. This hexagonal phase has different properties compared with the orthorhombic phase, such as multiferroicity and low magnetic-ordering temperature [15]. Canted antiferromagnetism with the spin reorientation transition is so far only reported for the orthorhombic phase. Until now, there has only been one report of TFO thin films grown on SrTiO₃ (STO) substrates that describes the structure as the standard perovskite structure, without characterization of their magnetic properties [14]. It is, then, at present not clear if thin films exhibit a spin structure and SRT similar to those found in the bulk, but understanding this is a key requirement in view of applications.

Here, we demonstrate that TFO does in fact grow in the bulk-like orthorhombic phase on STO, not in the cubic perovskite phase. Our thin films are of high crystallographic quality exhibiting oriented growth. We detect a canted moment and the spin reorientation transition similar to the bulk. Furthermore, we ascertain the direction of the Néel vector **N** and canted moment **M** in TFO thin films using SMR. We show how the spin reorientation can be read out electrically, thus being promising in view of applications such as providing a source of monochromatic terahertz radiation or data storage devices.

II. RESULTS AND DISCUSSION

Using the deposition parameters detailed in Sec. 1 of the Appendix, 200-nm-thick TFO_{*o*} films were deposited on (001)_{*p*}-oriented STO substrates. The subscripts *o* and *p*

*svenbecker@uni-mainz.de

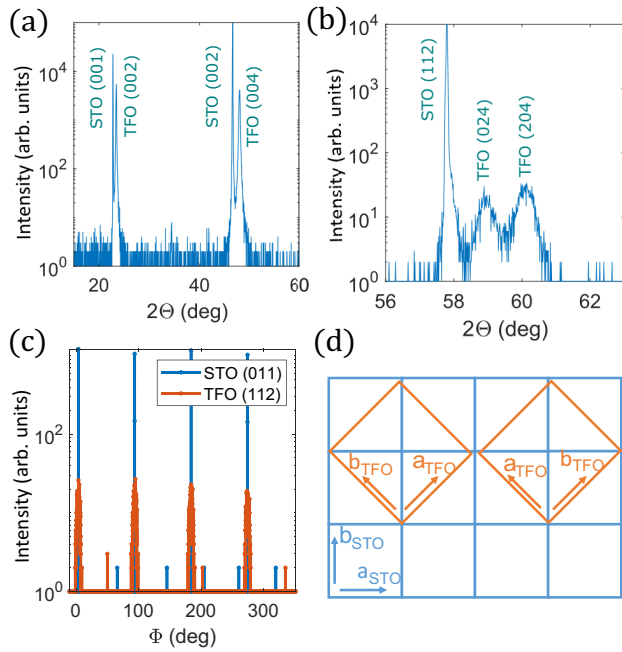


FIG. 1. (a) $2\Theta/\omega$ scan of a 200-nm TFO thin film grown on a STO (001)_p substrate measured out of plane. (b) $2\Theta/\omega$ measured along the (112)_p direction revealing both (024)_o and (204)_o TFO reflexes. (c) Φ scans with 2Θ fixed at STO (011)_p and TFO (112)_o reflexes. (d) Relative orientation of the TFO unit cells (orange) with respect to the STO surface (blue). Both configurations are present across the sample surface. The cell dimensions are to scale showing a good fit of the TFO *b* axis with the STO diagonal.

indicate the directions in an orthorhombic and perovskite unit cell, respectively. The crystallographic structure was investigated by making use of x-ray diffraction (XRD). An out-of-plane XRD scan in the range of $2\Theta = 15^\circ$ – 60° for a typical TFO sample is shown in Fig. 1(a). We observe (001)_p and (002)_p substrate and (002)_o and (004)_o TFO peaks with no additional impurity phase present. We calculate an out-of-plane lattice constant of 7.58 Å, which corresponds to the value of the bulk orthorhombic TFO *c* axis ($a = 5.25$ Å, $b = 5.57$ Å, and $c = 7.58$ Å) [16]. The other lattice parameters are determined by in-plane XRD measurements. A $2\Theta/\omega$ scan along the (112)_p direction gives the diffraction pattern shown in Fig. 1(b). Besides the (112)_p STO substrate peak, we find the (024)_o TFO peak at $2\Theta = 58.92^\circ$ and the (204)_o TFO peak at $2\Theta = 60.07^\circ$. To calculate the lattice parameters, we use the standard textbook formula for orthorhombic unit cells: $\frac{1}{d^2} = \frac{h^2}{a^2} + \frac{k^2}{b^2} + \frac{l^2}{c^2}$, where *d* is the spacing of diffraction planes calculated from the peak angle *h*, *k*, and *l* Miller indices and *c* is the lattice constant calculated from the out-of-plane XRD scan. We find $a = 5.28$ Å and $b = 5.57$ Å. The presence of both (024)_o and (204)_o diffraction peaks in one $2\Theta/\omega$ scan leads to the conclusion that there are two crystallographic domains with different in-plane orders present. The orthorhombic *b* axis of TFO is along the $\langle 110 \rangle_p$ of STO in one domain and along the $\langle \bar{1}10 \rangle_p$ in the other. The domains are separated by a 90° in-plane rotation of the unit cells. This is confirmed by Φ scans as shown in Fig. 1(c). We find that the (112)_o peaks in the Φ direction have a FWHM of 5.6° and reveal a fourfold

in-plane symmetry not consistent with the twofold symmetry expected from a single orthorhombic crystallographic domain. The (204)_o peak, on the other hand, has a FWHM of 4.3° , also revealing a fourfold in-plane symmetry (not shown). The smaller width of the (204)_o peaks compared with the (112)_o peaks in the Φ scans indicates that the orthorhombic *a* and *b* axes align with the STO diagonals leading to a distribution of orientations of the orthorhombic diagonal. The relative orientations are schematically shown in Fig. 1(d) for the unit cell of TFO (orange) atop the in-plane structure of the substrate (blue). Knowing the growth orientation of the TFO on STO, we determine a lattice mismatch of -4.9% for the TFO *a* axis and $+0.9\%$ for the TFO *b* axis, each corresponding to the diagonal of the STO *ab* plane. The sketch is made to scale so one can see that the TFO *b* axis fits the STO diagonal well. Our thin films clearly show the orthorhombic structure of bulk samples, which has not been reported before for thin films.

Having demonstrated the high-quality growth of TFO films in the orthorhombic phase on STO substrates, our attention now turns to the magnetic properties of the TFO thin films, which we investigated using superconducting quantum interference device (SQUID) magnetometry. Figure 2(a) shows a field cooled curve and a field warming curve for which the sample has been measured in out-of-plane (oop) and in-plane (ip) configurations along the orthorhombic axes, respectively. Details of the method can be found in Sec. 3 of the Appendix. The green region depicts the bulk spin reorientation region as measured in single crystals ($T_2 = 94$ K and $T_1 = 82$ K [17]), where the Néel vector **N** smoothly rotates between the two magnetic states [18]. Above the SRT, **N** is oriented in-plane along the orthorhombic *a* axis (Γ_4 phase). Since two crystallographic domains are present, **N** should lie in both possible in-plane directions 45° corresponding to the STO axes. In both cases, **M** is pointing along the *c* axis, which can be easily aligned in one direction using a magnetic field. Below the SRT the spins align along the *c* axis, and so **N** reorients out of the plane (Γ_2 phase). **M** can be directed in any of the four in-plane directions of the TFO *a* axis. These two possible configurations are shown for their respective temperature ranges in Fig. 2(d).

Focusing first on the SQUID oop measurement, the measured magnetization at high temperatures corresponds to the canted moment of the TFO, which increases slightly with decreasing temperature as can be explained by the parallel alignment of the paramagnetic Tm moments [19] or an increased canting angle. While the first effect is observed in bulk, the latter effect is not [20], but could occur in thin films due to temperature-dependent strain arising from different thermal-expansion coefficients of TFO and STO. Across the SRT, both **N** and **M** rotate smoothly to a new equilibrium position. Indeed, we note that the oop magnetization reaches a maximum around $T_{II} = 110$ K, which we attribute to the start of the SRT. As we continue to reduce the temperature, we note that the oop magnetization continues to decrease as **M** no longer lies along this direction. We reach a minimum for the magnetization at around 50 K, which stems from a superposition of the decreasing projection of **M** in the *c* direction and paramagnetic components increasing the signal at low temperatures. Therefore we make use of an ip measurement to determine the edge of the SRT. We observe a decreasing

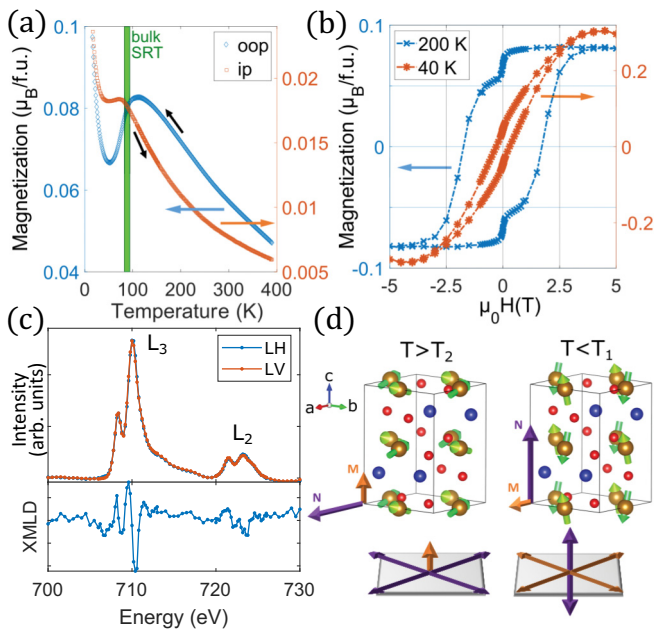


FIG. 2. (a) Magnetization vs temperature for out-of-plane (oop, along the c axis) and in-plane (ip, along the orthorhombic a axis, 45° towards the STO axis) configurations. The bulk spin reorientation transition is depicted in green. (b) Field sweep with field applied in the oop direction along the c axis with a maximum applied field of 5 T. The data have been corrected for para- and diamagnetic background. (c) Top: XAS for linear horizontal (LH) and linear vertical (LV) polarization measured at 300 K. Bottom: XMLD spectrum calculated as the difference between LV and LH. (d) The magnetic configuration of the TFO unit cell above (left) and below (right) the spin reorientation transition drawn in VESTA [24]. Due to the presence of two crystallographic domains the a axis can be aligned in two directions leading to the magnetic configuration of the overall sample as sketched below corresponding to the cubic STO surface. The Néel N vector is shown in purple, and the canted moment M is shown in orange.

magnetic moment along the a axis above $T_1 = 72$ K when measuring along the substrate diagonal, which we attribute to the end of the SRT.

These measurements indicate that the SRT is present in our thin films. This shows that they exhibit the desired magnetic properties as the SRT is similar to bulk samples. We note that $T_1 = 72$ K and $T_{II} = 110$ K deviate slightly from the bulk values $T_1 = 82$ K and $T_2 = 94$ K. The extension of the SRT to $T_I = 82$ K and $T_2 = 120$ K in near-surface regions has been reported in Ref. [21] for bulk samples. A further increase in the SRT region may stem from the small size of the TFO grains and the resulting enlarged surface area. There is also the probability that the strain, induced by the thin film growth, alters the key magnetic anisotropies along the a and c axes responsible for the transition, as has been demonstrated for SmFeO_3 [22].

To confirm our observations, we next perform measurements of the magnetization as a function of the applied magnetic field at a constant temperature above (200 K) and below (40 K) our observed SRT. Once the background from the diamagnetic substrate and paramagnetic components has

been subtracted [see Fig. 2(b)], we observe a curve consisting of two contributions for an oop magnetic field at 200 K: a broad hysteresis with a coercive field of 1.8 T and a soft hysteresis at very low magnetic fields. For the 40-K curve, the soft hysteresis around 0 T is still present. The second contribution to the signal has adopted a shape more reminiscent of a hard-axis ferromagnetic loop than an easy-axis as expected. From low-amplitude hysteresis loops discussed in Sec. 4 of the Appendix we observe that the soft-magnetic contribution is temperature independent and therefore not linked to the magnetic structure of the orthorhombic TFO. Subtracting the soft-magnetic contribution, the saturation magnetization at 200 K is found to be around $0.06 \mu_B/f.u.$, which is lower than the value of around $0.085 \mu_B/f.u.$ which was recently reported on TFO bulk samples also using $M(H)$ measurements [23]. The magnitude of the saturation magnetization has two contributions: the paramagnetic T_m moments being polarized by the local crystal field generated by the Fe atoms and the canting of the Fe sublattices, which is related to the strength of the antisymmetric exchange interaction [Dzyaloshinskii-Moriya interaction (DMI)] present in all rare-earth orthoferrites [20]. The crystallographic distortion due to strain affects the crystal field, thus leading to deviations of the DMI through higher-order terms of the spin-orbit coupling. Therefore a deviation between magnetization values of bulk and thin films samples is not surprising.

We have demonstrated by SQUID measurements that our films have a measurable SRT signal. We have assumed that our samples fulfill the model of a canted antiferromagnet. However, we have yet to show that our films actually possess antiferromagnetic ordering to rule out the possibility that the SQUID signals stem from ferromagnetic impurities. In order to confirm that they are antiferromagnetic, x-ray absorption spectra (XAS) were measured for circular and linear polarized photons around the Fe L_2 and L_3 edges at the Diamond Light Source I06 beamline. The x-ray magnetic circular dichroism (XMCD) and x-ray magnetic linear dichroism (XMLD) were calculated. Details on the method and the XMCD spectrum are given in Sec. 5 of the Appendix. We note that there is no clear XMCD signal measured when using circularly polarized x-rays. The lack of XMCD means that in the near-surface region we do not observe evidence of a ferromagnetic phase or the canted moment. The missing of the latter is likely due to the sensitivity limit of the technique. This is not surprising given its small magnitude and the finite sensitivity of the setup, as well as the difficulties in measuring out-of-plane magnetism with x-rays having a grazing incidence angle of 16° . In order to demonstrate the antiferromagnetic nature of our films, we take XAS for horizontal and vertical linearly polarized x-rays. The XMLD is calculated as $\text{XMLD} = I_{LH} - I_{LV}$, where I_{LH} and I_{LV} are the XAS for horizontal and vertical linear polarization, respectively. The parallel (perpendicular) component of the Néel vector will give rise to a decrease (increase) in the XAS. We show in Fig. 2(c) the XAS and XMLD spectra calculated at 300 K, where clear dichroism is visible at both the Fe L_2 and L_3 edges. The clear presence of XMLD and absence of XMCD demonstrate that our films are indeed antiferromagnetic. The investigation of our TFO/STO thin films has shown that TFO grows in the orthorhombic phase like bulk crystals. These films show the typical TFO features such

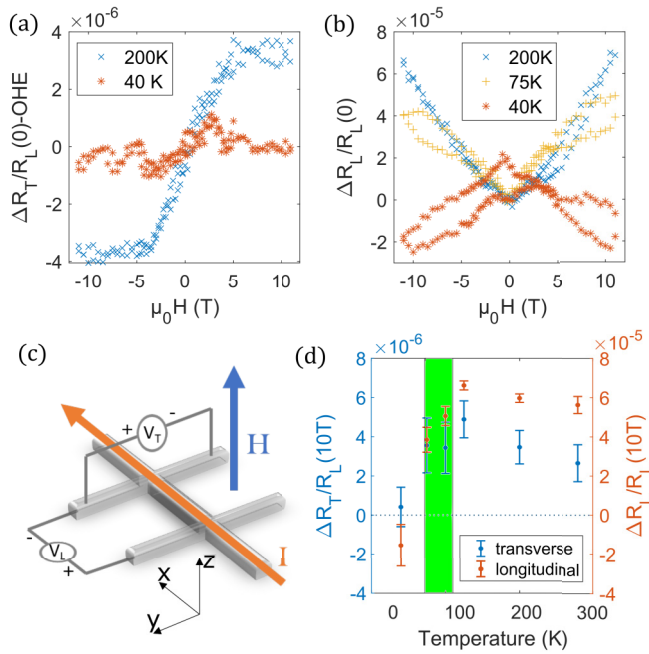


FIG. 3. (a) Transverse spin Hall magnetoresistance (SMR) as a function of magnetic field at a temperature of 200 and 40 K. The field is applied in the z direction (out of the plane). Note that the transverse SMR is extracted by subtracting the ordinary Hall effect from the measured transverse resistivity. A floating average has been applied with a range over 1 T to smooth the data. (b) Relative longitudinal resistivity measured simultaneously. (c) Sketch of the measurement configuration, with the coordinate system of the Hall bar indicated. (d) Amplitude of transverse and longitudinal relative resistivity at 10 T. The spin reorientation transition determined by SQUID measurements is depicted in green.

as antiferromagnetic ordering and a SRT. However, we have so far used bulk techniques to detect this ordering. Device applications necessitate the all-electrical, on-chip detection of the AFM ordering and SRT, for which we turn to spin Hall magnetoresistance [25].

Using lithographic methods, we define Pt Hall bars as detailed in Sec. 1 of the Appendix in order to electrically investigate the reorientation of the magnetic structure with temperature. The Hall bars are aligned parallel to the STO a axis and thus make a 45° angle to the film a and b axes. z is perpendicular to the Hall bar out of the plane, which coincides with the orthorhombic c direction [see Fig. 3(c)]. The electrical properties of the Pt Hall bar are further described in Sec. 6 of the Appendix.

We pass a charge current along x through the Pt, which leads to a spin accumulation μ_s at the Pt/TFO interface polarized along y , while capturing a longitudinal and transverse resistivity as a function of the magnetic field applied along z . The interaction between μ_s and the magnetic order parameters, which can be \mathbf{N} [10,26] or \mathbf{M} [27], leads to a modulation of the Pt resistance due to the spin Hall magnetoresistance (SMR). Changes in the orientation of \mathbf{N} and \mathbf{M} then lead to an electrically detectable response. The longitudinal resistivity can be plagued by numerous additional effects such as ordinary magnetoresistance [28], Hanle magnetoresistance

[29], and sensitivity to small temperature changes, which may be comparable to, or even mask, the small effect of the SMR. On the other hand, the interpretation of the transverse resistivity R_T data is more straightforward. With a field applied in the z direction, R_T has two key contributions: the ordinary Hall effect (OHE) [30] and the spin Hall anomalous Hall effect (SHAHE), which is related to the z component of the magnetization of the material in contact with the conductor [31]. Other effects such as the planar Hall effect [32], anomalous Hall effect [30], magnetic spin Hall effect [33], and topological Hall effect [34] are only relevant for magnetic conductors and can be discarded here, where we consider an antiferromagnetic insulator. The OHE arises as a linearly increasing change in resistance with magnetic field making it simple to account for. In the case of an antiferromagnet without a significant canted moment, only the OHE is expected. However, we observe a distinct S shape in the transverse resistivity beneath the linear contribution from the OHE at 200 K [Fig. 3(a)]. We note that the S shape saturates at a similar magnetic field magnitude as the hysteresis observed previously by SQUID. To determine further whether this hysteresis originates from the TFO films, we cool below the SRT to 40 K, where the canted moment now lies in plane. While the contribution from OHE remains unchanged, the S shape disappears, confirming that this signal originates from the net magnetic moment of the TFO films. This is shown in Fig. 3(a). Given that, ignoring the Néel vector, the transverse resistivity is proportional to the z component of the magnetization [31,35], we attribute this hysteresis to the SHAHE [31,36] of the canted moment \mathbf{M} oriented along z . Unlike in the SQUID measurements [Fig. 2(b)], a remnant magnetization in R_T is not observed above the SRT. A fundamentally different spin configuration at the surface layer compared with bulk is not expected since previous experiments on bulk samples underline the similarity of surface-sensitive and bulk measurements [21,37,38]. The absence of a remnant signal may arise from the broken inversion symmetry at the TFO/Pt interface competing with the bulk DMI, reducing the canted moment at the interface. The absence of a canted moment leads to the vanishing of the signal at zero field. We note that the absence of a ferromagnetic moment at the Pt/TFO interface was also indicated by our XMCD measurements. The soft hysteresis observed in SQUID, which may stem from a maghemite phase, has no obvious impact on the measurement. We also note that the signal has the same symmetry as the proximity-induced anomalous Hall effect (AHE). However, we do not expect the proximity effect in our samples as it is not observed in other Pt/AFM heterostructures either [39] given the lack of a large net magnetic moment and stray fields. We therefore suggest that the transverse signal is dominated by the orientation of \mathbf{M} , specifically the z component, reminiscent of the SHAHE observed in ferromagnets. The dominance of the magnetic spin mixing conductance in the transverse signal would indicate that the magnetic spin mixing conductance should also dominate the longitudinal response [Fig. 3(b)]. In fact, we do see a significant change in the longitudinal resistivity as a function of magnetic field when going through the SRT. The amplitude clearly decreases with decreasing temperature around the SRT. Within the transition we see an intermediate state which might indicate the magnetic-field-induced reorientation

of \mathbf{M} and \mathbf{N} [40]. This would indicate a R_L dependence on \mathbf{M} , having a positive magnetoresistive (MR) effect together with a decrease in M_y and an increase in the N_y contribution. Assuming this dependence and ignoring other effects, one would expect no MR effect at 200 K, because \mathbf{M} does not have a y contribution above the SRT. However, we observe a large positive MR that could be explained by the dependence of R_L on \mathbf{N} . Therefore clearly identifying the dependence of R_L on \mathbf{M} or \mathbf{N} is challenging and needs further measurements, also to identify the contributions from temperature and other MR effects, i.e., ordinary MR (OMR) and Hanle MR, which have the same symmetry as SMR in our measurement geometry.

In summary, we observe a strong change in both R_T and R_L through the SRT. The dependence of the signal amplitude with temperature is shown in Fig. 3(d). The amplitude of R_T follows our expectations centered around a dominant contribution from M_z and the associated SHAHE; however, the dependence of R_L cannot be explained through only the y component of either \mathbf{N} or \mathbf{M} . Instead, the behavior appears to be in a certain sense related to the out-of-plane component of the magnetization. However, this is not consistent with the present description of SMR [25,31] and would require further study of the SMR in canted AFMs with a significant DMI that goes beyond the scope of this work.

III. CONCLUSION

We have successfully grown samples of oriented orthorhombic TmFeO_3 thin films on SrTiO_3 substrates by pulsed laser deposition. We observe a fourfold symmetry of the in-plane ordering due to the cubic symmetry of the substrate resulting in crystallographic twinning. The samples exhibit antiferromagnetic ordering, a canted moment, and a spin reorientation transition (SRT), as confirmed by SQUID magnetometry and XMLD. The SRT is shifted compared with bulk samples due to strained growth altering the local crystal field. To detect the SRT electrically, we utilize spin Hall magnetoresistance (SMR). We can ascertain the different magnetic phases utilizing SHAHE and also observe anomalies in the longitudinal SMR signal going through the SRT. The surface-sensitive nature of SMR overcomes the need for bulk measurements, which can, for thinner films, be difficult due to the small volume and substrate contributions. Our results demonstrate that one can electrically detect the spin reorientation transition of canted antiferromagnetic orthoferrites, which is important for future spintronic applications such as memory devices and canted antiferromagnetic nano-oscillators.

ACKNOWLEDGMENTS

The authors gratefully acknowledge funding by Deutsche Forschungsgemeinschaft (DFG, German Research Foundation) Project No. 358671374. This work was supported by the Max Planck Graduate Center with the Johannes Gutenberg-Universität Mainz (MPGC) as well the Graduate School of Excellence Materials Science in Mainz (GSC266). This work was funded by DFG Grant No. TRR 173 Spin+X A01 268565370 and KAUST Grant No. OSR-2019-CRG8-4048.2 and FET-open s-Nebula (No. 863155). L.B. acknowledges the European Union's Horizon 2020 research and innovation

TABLE I. Deposition conditions for PLD of TFO thin films.

Parameter	Value
Deposition temperature ($^{\circ}\text{C}$)	630
O_2 pressure (mbar)	0.2
Substrate-target distance (cm)	5.5
Laser energy per pulse (mJ)	130
Laser spot size (mm^2)	9
Laser pulse frequency (Hz)	10
Cooling rate after deposition (K/min)	25
Growth rate (nm/min)	1.6

program under Marie Skłodowska-Curie Grant Agreement ARTES No. 793159. We acknowledge Diamond Light Source for time on beamline I06 under Proposal No. MM23819.

APPENDIX

1. Methods

A TmFeO_3 target was prepared by standard solid-state reaction out of Tm_2O_3 and Fe_2O_3 powder. Thin films were prepared by pulsed laser deposition (PLD) on SrTiO_3 (001) substrates using a KrF COMPexPro 205 excimer laser and a vacuum chamber with a base pressure of 2×10^{-8} mbar (see Table I). The STO substrates were prepared by standard HF etching procedure for TiO_2 termination [41]. The structural properties of the samples were investigated using x-ray diffraction (XRD) and a Bruker D8 four-circle diffractometer with a Cu anode, equipped with a monochromator to suppress Cu K_{β} radiation. The temperature-dependent magnetic properties were analyzed using a superconducting quantum interference device (SQUID) from Quantum Design. The surface morphology was imaged using atomic force microscopy (AFM) with a Digital Instruments 3100 Dimension equipped with a NanoScope IV controller. As probes, Bruker SNL-10 were used. For plotting the images and calculating the grain size, GWYDDION software [42] was utilized.

For the transport measurements, platinum Hall bars were defined by lithographic methods, with Pt deposited using DC magnetron sputtering at room temperature and a lift-off process. The dimensions of the Hall bars are $10 \mu\text{m}$ in width, 7 nm in thickness, and $100 \mu\text{m}$ in length. The arms are separated by $55 \mu\text{m}$ and have a width of $3 \mu\text{m}$. Electrical measurements at a Hall bar were performed in a cryostat equipped with a variable-temperature insert. Magnetic fields up to 11 T and temperatures in the range of 5–300 K can be accessed. A sample identical to that utilized for transport measurements was covered by 2 nm of Pt in order to prevent charging and measured at Diamond Light Source beamline I06. Before measuring the x-ray absorption spectra (XAS) the sample was put in a magnetic field of 5 T applied in the c direction. XAS were measured around the L_3 and L_2 iron absorption edges.

2. AFM

The surface of the sample was investigated by atomic force microscopy. The data of a $5 \times 5 \mu\text{m}$ scan were analyzed with GWYDDION software [42]. An image of the topography is

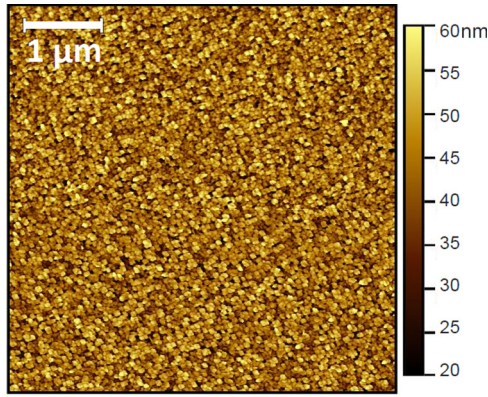


FIG. 4. Atomic force microscopy image of the sample surface. The scale bar corresponds to $1 \mu\text{m}$.

shown in Fig. 4. We determine an overall root-mean-square (RMS) roughness (Sq) of around 8 nm for a film thickness of 200 nm. The size of the surface grains was calculated by masking the grains using a height threshold of 43%, resulting in a mean grain size of 42 nm. We suggest that the grain size could be increased by making use of substrates without the cubic symmetry of STO to prevent the formation of twinned domains (e.g., DyScO_3 , NdGaO_3 , YAlO_3 , or related orthorhombic materials). While this is not of relevance for the work here, where the transport measurements are integrating over areas far larger than the individual grain size, other branches of antiferromagnetic spintronics can benefit from a reduction in grain and magnetic domain boundaries [43].

3. SQUID M versus T curves

The measurement of the SRT was performed in the SQUID, measuring the temperature-dependent magnetization along the TFO c and a axes as shown in the main text. For the oop measurement (along the c axis) the sample was heated up to 390 K. At this temperature a field magnitude of 5 T was briefly applied along the c axis to align \mathbf{M} of the individual domains. Then a field of 30 mT was applied, and the temperature-dependent magnetization was measured during cooldown at a rate of 2 K/min. For the ip measurement, a magnetic field of 5 T was applied 45° to the STO in-plane axes, which is along the crystallographic a and b TFO axis for the two different domains, respectively. The field was applied at a temperature of 20 K for a short period of time, again to saturate the canted moment. The sample was then heated in a magnetic field of 50 mT at 2 K/min. Here, a larger magnetic field was chosen because at lower fields, ferro-, para-, and diamagnetic contributions compensate at some point in the measurement range. This leads to the measurement software not being able to fit the raw signal, which further leads to jumps in the $M(T)$ curve that are not originating from the sample's properties.

4. SQUID minor loops

We investigate the soft-magnetic phase by taking minor loops around 0 T so as to exclude the high-field contributions.

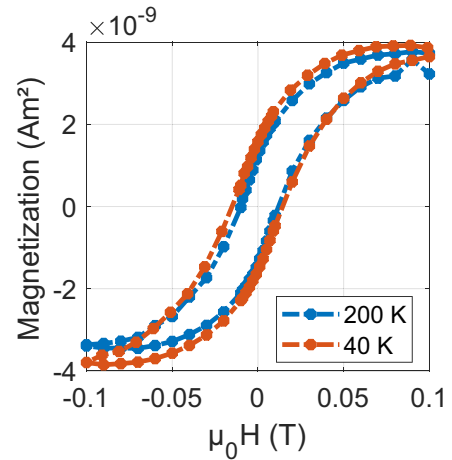


FIG. 5. Minor loop measured in SQUID in the out-of-plane configuration at different temperatures with a maximum applied field of 0.1 T. Note that the scale cannot be normalized because of the unknown volume of the soft-magnetic phase. The data have been corrected for para- and diamagnetic background.

This is done by first applying a field of -5 T to the sample for a short period of time. Then the $M(H)$ loop is measured with $H_{\text{max}} = 0.1$ T starting from positive values. We observe a hysteresis that has a coercive field of 12 mT (18 mT) and a maximum magnetic moment of $3.6 \times 10^{-9} \text{ A m}^2$ ($3.8 \times 10^{-9} \text{ A m}^2$) at a temperature of 200 K (40 K). This contribution does not change significantly with temperature as shown in Fig. 5. Note that the values for the magnetization are not normalized because the volume of the soft-magnetic phase is unknown. Hysteresis curves with soft- and hard-magnetic contributions are referred to in the literature as wasp-waisted hysteresis loops. They have already been reported for other oxides such as CoFe_2O_4 thin films [44–46] and $\text{Fe}_3\text{O}_4/\text{CoO}$ bilayers [47]. For polycrystalline orthoferrite thin films (not TFO), there are reports of strange phases leading to a soft hysteresis [48,49]. Possible phases which are named are a garnet phase, magnetite (Fe_3O_4), and rare-earth oxide. For TFO the corresponding garnet phase is $\text{Tm}_3\text{Fe}_5\text{O}_{12}$ (TIG), an insulating ferrimagnet, whose magnetization changes by a factor of around 3 between 200 and 40 K [50]. Magnetite possesses a phase transition at 125 K below which the coercivity increases drastically [51], and Tm_2O_3 is a paramagnetic material [52]. So none of these candidates seem to explain the similarity of the soft-magnetic contributions at 40 and 200 K in our TFO thin films. For hematite ($\alpha\text{-Fe}_2\text{O}_3$), a related compound to orthoferrites, thin films possess a thin maghemite ($\gamma\text{-Fe}_2\text{O}_2$) layer at the substrate interface [53]. If we assume such a layer in our sample, the magnetic signal corresponds to a maghemite volume fraction of 0.2% of the whole TFO layer thickness. We cannot exclude the presence of this phase from XRD measurements since the count rate of such a small volume is around the noise level in our setup, even if it was well oriented. Nevertheless, we see that the impact on electric measurements by the soft-magnetic phase, whether maghemite or not, is negligible for our studies.

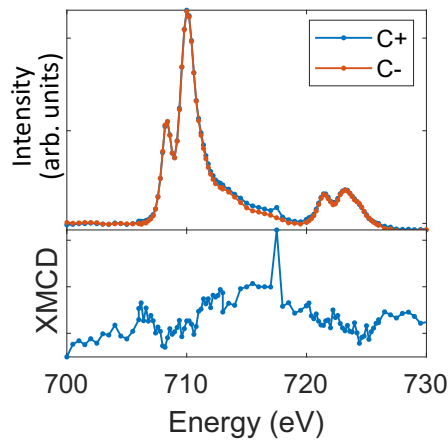


FIG. 6. Top: x-ray absorption spectra for circular polarized photons C+ and C-. Bottom: XMCD spectrum calculated as the difference between C+ and C-.

5. XMLD

In order to confirm that our TFO thin films are anti-ferromagnetic, XAS were captured at the Fe $L_{2/3}$ edge for linear horizontal (LH) and vertical (LV) polarization as well as positive (C+) and negative circular (C-) polarization. The sample was aligned with the orthorhombic axes in the reflection plane. The incident angle of the beam was 16° . The data were processed as follows: The reflected intensity was divided by the incident intensity of the x-ray beam to account for modulation of the incoming intensity. The background away from the L_2 and L_3 peaks was subtracted to shift the baseline to zero of each curve. A correction factor was multiplied with LH and C+ to align LH and LV as well as the C+ and C- curves. XMLD and XMCD are calculated by $\text{XMLD} = I_{\text{LH}} - I_{\text{LV}}$ and $\text{XMCD} = I_{\text{C+}} - I_{\text{C-}}$. The XMCD spectrum is shown in Fig. 6, while the XMLD spectrum is shown in the main text. While for the XMLD spectrum we observe a clear signal around the L_3 edge, there is no clear signal to be identified in the XMCD spectrum. The

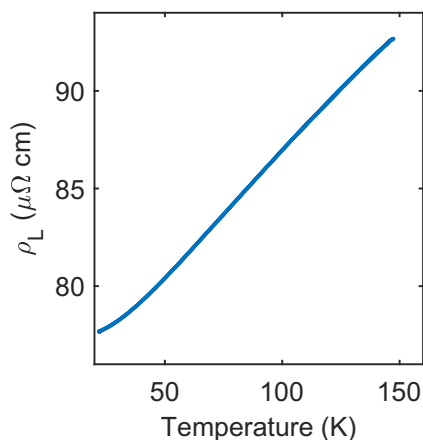


FIG. 7. Temperature-dependent resistivity of the Pt Hall bar in the absence of a magnetic field.

lack of XMCD means that in the near-surface region we do not observe evidence of a ferromagnetic phase or the canted moment.

6. Pt Hall bar

The requirements for the Pt Hall bar are that it must be sufficiently thick to be electrically conducting but not too thick to suppress the SMR signal. In yttrium iron garnet (YIG)/Pt bilayers, an optimal thickness of around twice the spin relaxation length has been determined [54]. However, due to the roughness of our TFO/STO sample, we chose a higher thickness to ensure that the first requirement is satisfied. The temperature-dependent resistivity in the absence of a magnetic field is shown in Fig. 7 for the temperature range between around 20 and 150 K. The behavior clearly indicates metallic conductance of the Pt Hall bar leading to the conclusion that the Pt layer is continuous and allows for SMR measurements. From this figure, we also see that the SRT is not observable from temperature-dependent resistivity measurements, likely due to the small magnitude of the SMR signal compared with the temperature-dependent resistivity of the Pt itself.

When performing $R(H)$ measurements as described in the main text, the major contribution of the transverse signal is due to the OHE from the Pt wire itself, originating in the Lorentz force acting on the charge carriers. The OHE shows a small temperature dependence as seen in Pt/gadolinium gallium garnet (GGG) samples [55,56]. Therefore, to account for the purely linear OHE, a linear fit is taken at large magnetic field values and subtracted from the data in order to leave any nonlinear contributions. All corrections are of the order of $7 \times 10^{-6} \text{ T}^{-1}$, in units of relative transverse resistance change normalized to the zero-field longitudinal resistivity. However, this leads to a subtraction of all linear contributions, including possible linear effects of the SMR. This also means that any contribution to the SMR due to field-induced spin rotation of the sublattices under an applied field, which can also have a close-to-linear dependence as shown in Mössbauer studies for the similar orthoferrites ErFeO_3 [57] and YFeO_3 [58], is thereby excluded. Also, the approximately linear field-induced increase in canting angle [59] is thereby not visible in the transverse resistivity data. These effects would become visible only when reaching a complete spin reorientation at a sufficiently large magnetic field applied perpendicular to \mathbf{M} . We would expect, then, in the electrical measurements to observe two linear regimes—one from the OHE + the hard-axis magnetization and a second from the OHE + sublattice canting—however, this is not visible above the noise. There are two possible explanations: Either the spin-flop field is not reached, or the increase in canting angle contributes by the same magnitude to M_z as the rotation of \mathbf{M} , and we do not see two regimes. However, these effects are beyond the scope of this paper. Here, we investigate the principle of determining the spin state of TFO by electrical means and therefore focus on the nonlinear contribution of transverse resistivity R_T stemming from the switching of M_z .

- [1] V. Baltz, A. Manchon, M. Tsoi, T. Moriyama, T. Ono, and Y. Tserkovnyak, Antiferromagnetic spintronics, *Rev. Mod. Phys.* **90**, 015005 (2018).
- [2] T. Jungwirth, X. Marti, P. Wadley, and J. Wunderlich, Antiferromagnetic spintronics, *Nat. Nanotechnol.* **11**, 231 (2016).
- [3] T. Jungwirth, J. Sinova, A. Manchon, X. Marti, J. Wunderlich, and C. Felser, The multiple directions of antiferromagnetic spintronics, *Nat. Phys.* **14**, 200 (2018).
- [4] O. R. Sulymenko, O. V. Prokopenko, V. S. Tiberkevich, A. N. Slavina, B. A. Ivanov, and R. S. Khymyn, Terahertz-Frequency Spin Hall Auto-Oscillator Based on a Canted Antiferromagnet, *Phys. Rev. Appl.* **8**, 064007 (2017).
- [5] P. Stremoukhov, A. Safin, M. Logunov, S. Nikitov, and A. Kirilyuk, Spintronic terahertz-frequency nonlinear emitter based on the canted antiferromagnet-platinum bilayers, *J. Appl. Phys.* **125**, 223903 (2019).
- [6] P. Wadley, B. Howells, J. Železný, C. Andrews, V. Hills, R. P. Campion, V. Novák, K. Olejnik, F. Maccherozzi, S. S. Dhesi, S. Y. Martin, T. Wagner, J. Wunderlich, F. Freimuth, Y. Mokrousov, J. Kuneš, J. S. Chauhan, M. J. Grzybowski, A. W. Rushforth, K. W. Edmonds *et al.*, Electrical switching of an antiferromagnet, *Science* **351**, 587 (2016).
- [7] S. Schlauderer, C. Lange, S. Baierl, T. Ebnet, C. P. Schmid, D. C. Valovcin, A. K. Zvezdin, A. V. Kimel, R. V. Mikhaylovskiy, and R. Huber, Temporal and spectral fingerprints of ultrafast all-coherent spin switching, *Nature* **569**, 383 (2019).
- [8] M. Jourdan, H. Bräuning, A. Sapozhnik, H.-J. Elmers, H. Zabel, and M. Kläui, Epitaxial Mn_2Au thin films for antiferromagnetic spintronics, *J. Phys. D: Appl. Phys.* **48**, 385001 (2015).
- [9] C. Mix and G. Jakob, Multiferroic and structural properties of $BiFeO_3$ close to the strain induced phase transition on different substrates, *J. Appl. Phys.* **113**, 17D907 (2013).
- [10] L. Baldrati, O. Gomonay, A. Ross, M. Filianina, R. Lebrun, R. Ramos, C. Leveille, F. Fuhrmann, T. R. Forrest, F. Maccherozzi, S. Valencia, F. Kronast, E. Saitoh, J. Sinova, and M. Kläui, Mechanism of Néel Order Switching in Antiferromagnetic Thin Films Revealed by Magnetotransport and Direct Imaging, *Phys. Rev. Lett.* **123**, 177201 (2019).
- [11] T. Moriyama, K. Oda, T. Ohkochi, M. Kimata, and T. Ono, Spin torque control of antiferromagnetic moments in NiO , *Sci. Rep.* **8**, 14167 (2018).
- [12] S.-J. Ahn, J.-H. Lee, H. M. Jang, and Y. K. Jeong, Multiferroism in hexagonally stabilized $TmFeO_3$ thin films below 120 K, *J. Mater. Chem. C* **2**, 4521 (2014).
- [13] L. Jin, Y. He, D. Zhang, H. Zhang, M. Wei, and Z. Zhong, Near-ultraviolet photodetector based on hexagonal $TmFeO_3$ ferroelectric semiconductor thin film with photovoltaic and pyroelectric effects, *APL Mater.* **7**, 121105 (2019).
- [14] A. A. Bossak, I. E. Graboy, O. Y. Gorbenko, A. R. Kaul, M. S. Kartavtseva, V. L. Svetchnikov, and H. W. Zandbergen, XRD and HREM studies of epitaxially stabilized hexagonal orthoferrites $RFeO_3$ ($R = Eu-Lu$), *Chem. Mater.* **16**, 1751 (2004).
- [15] A. R. Akbashev, A. S. Semisalova, N. S. Perov, and A. R. Kaul, Weak ferromagnetism in hexagonal orthoferrites $RFeO_3$ ($R=Lu, Er-Tb$), *Appl. Phys. Lett.* **99**, 122502 (2011).
- [16] M. Marezio, J. P. Remeika, and P. D. Dernier, The crystal chemistry of the rare earth orthoferrites, *Acta Cryst. Sect. B* **26**, 2008 (1970).
- [17] J. Leake, G. Shirane, and J. Remeika, The magnetic structure of thulium orthoferrite, $TmFeO_3$, *Solid State Commun.* **6**, 15 (1968).
- [18] R. Wolfe, R. D. Pierce, S. E. Haszko, and J. P. Remeika, Temperature-induced spin reorientation in rare earth orthoferrites—hysteresis loop studies, *Appl. Phys. Lett.* **11**, 245 (1967).
- [19] R. L. White, Review of recent work on the magnetic and spectroscopic properties of the rare-earth orthoferrites, *J. Appl. Phys.* **40**, 1061 (1969).
- [20] D. Treves, Studies on orthoferrites at the Weizmann Institute of Science, *J. Appl. Phys.* **36**, 1033 (1965).
- [21] U. Staub, L. Rettig, E. M. Bothschafter, Y. W. Windsor, M. Ramakrishnan, S. R. V. Avula, J. Dreiser, C. Piamonteze, V. Scagnoli, S. Mukherjee, C. Niedermayer, M. Medarde, and E. Pomjakushina, Interplay of Fe and Tm moments through the spin-reorientation transition in $TmFeO_3$, *Phys. Rev. B* **96**, 174408 (2017).
- [22] M. Kuroda, N. Tanahashi, T. Hajiri, K. Ueda, and H. Asano, Strain effect on magnetic property of antiferromagnetic insulator $SmFeO_3$, *AIP Adv.* **8**, 055814 (2018).
- [23] J.-S. Zhou, L. G. Marshall, Z.-Y. Li, X. Li, and J.-M. He, Weak ferromagnetism in perovskite oxides, *Phys. Rev. B* **102**, 104420 (2020).
- [24] K. Momma and F. Izumi, *VESTA3* for three-dimensional visualization of crystal, volumetric and morphology data, *J. Appl. Cryst.* **44**, 1272 (2011).
- [25] H. Nakayama, M. Althammer, Y.-T. Chen, K. Uchida, Y. Kajiwara, D. Kikuchi, T. Ohtani, S. Geprägs, M. Opel, S. Takahashi, R. Gross, G. E. W. Bauer, S. T. B. Goennenwein, and E. Saitoh, Spin Hall Magnetoresistance Induced by a Nonequilibrium Proximity Effect, *Phys. Rev. Lett.* **110**, 206601 (2013).
- [26] R. Lebrun, A. Ross, O. Gomonay, S. A. Bender, L. Baldrati, F. Kronast, A. Qaiumzadeh, J. Sinova, A. Brataas, R. A. Duine, and M. Kläui, Anisotropies and magnetic phase transitions in insulating antiferromagnets determined by a spin-Hall magnetoresistance probe, *Commun. Phys.* **2**, 50 (2019).
- [27] T. Hajiri, L. Baldrati, R. Lebrun, M. Filianina, A. Ross, N. Tanahashi, M. Kuroda, W. L. Gan, T. O. Mentş, F. Genuzio, A. Locatelli, H. Asano, and M. Kläui, Spin structure and spin Hall magnetoresistance of epitaxial thin films of the insulating non-collinear antiferromagnet $SmFeO_3$, *J. Phys.: Condens. Matter* **31**, 445804 (2019).
- [28] M. Isasa, S. Vélez, E. Sagasta, A. Bedoya-Pinto, N. Dix, F. Sánchez, L. E. Hueso, J. Fontcuberta, and F. Casanova, Spin Hall Magnetoresistance as a Probe for Surface Magnetization in $Pt/CoFe_2O_4$ Bilayers, *Phys. Rev. Appl.* **6**, 034007 (2016).
- [29] S. Vélez, V. N. Golovach, A. Bedoya-Pinto, M. Isasa, E. Sagasta, M. Abadia, C. Rogero, L. E. Hueso, F. S. Bergeret, and F. Casanova, Hanle Magnetoresistance in Thin Metal Films with Strong Spin-Orbit Coupling, *Phys. Rev. Lett.* **116**, 016603 (2016).
- [30] R. Karplus and J. M. Luttinger, Hall effect in ferromagnetics, *Phys. Rev.* **95**, 1154 (1954).
- [31] Y.-T. Chen, S. Takahashi, H. Nakayama, M. Althammer, S. T. B. Goennenwein, E. Saitoh, and G. E. W. Bauer, Theory of spin Hall magnetoresistance (SMR) and related phenomena, *J. Phys.: Condens. Matter* **28**, 103004 (2016).

- [32] A. Taskin, H. F. Legg, F. Yang, S. Sasaki, Y. Kanai, K. Matsumoto, A. Rosch, and Y. Ando, Planar Hall effect from the surface of topological insulators, *Nat. Commun.* **8**, 1340 (2017).
- [33] M. Kimata, H. Chen, K. Kondou, S. Sugimoto, P. K. Muduli, M. Ikhlas, Y. Omori, T. Tomita, A. H. MacDonald, S. Nakatsuji, and Y. Otani, Magnetic and magnetic inverse spin Hall effects in a non-collinear antiferromagnet, *Nature* **565**, 627 (2019).
- [34] B. Binz and A. Vishwanath, Chirality induced anomalous-Hall effect in helical spin crystals, *Physica B: Condens. Matter* **403**, 1336 (2008).
- [35] N. Vlietstra, J. Shan, V. Castel, J. B. Youssef, G. E. W. Bauer, and B. J. van Wees, Exchange magnetic field torques in YIG/Pt bilayers observed by the spin-Hall magnetoresistance, *Appl. Phys. Lett.* **103**, 032401 (2013).
- [36] Y.-T. Chen, S. Takahashi, H. Nakayama, M. Althammer, S. T. B. Goennenwein, E. Saitoh, and G. E. W. Bauer, Theory of spin Hall magnetoresistance, *Phys. Rev. B* **87**, 144411 (2013).
- [37] E. A. Balykina, E. A. Gan'shina, and G. S. Krinichik, Magneto-optic properties of rare-earth orthoferrites in the region of spin reorientation transitions, *Zh. Eksp. Teor. Fiz.* **93**, 1879 (1987) [*Sov. Phys. JETP* **66**, 1073 (1987)].
- [38] G. Gorodetsky, S. Shaft, and J. P. Remeika, Propagation of surface magnetoelastic waves in TmFeO_3 at the spin reorientation, *J. Appl. Phys.* **52**, 7353 (1981).
- [39] T. Shang, Q. F. Zhan, H. L. Yang, Z. H. Zuo, Y. L. Xie, L. P. Liu, S. L. Zhang, Y. Zhang, H. H. Li, B. M. Wang, Y. H. Wu, S. Zhang, and R.-W. Li, Effect of NiO inserted layer on spin-Hall magnetoresistance in Pt/NiO/YIG heterostructures, *Appl. Phys. Lett.* **109**, 032410 (2016).
- [40] R. C. LeCraw, R. Wolfe, E. M. Gyorgy, F. B. Hagedorn, J. C. Hensel, and J. P. Remeika, Microwave absorption near the reorientation temperature in rare earth orthoferrites, *J. Appl. Phys.* **39**, 1019 (1968).
- [41] G. Koster, B. L. Kropman, G. J. H. M. Rijnders, D. H. A. Blank, and H. Rogalla, Quasi-ideal strontium titanate crystal surfaces through formation of strontium hydroxide, *Appl. Phys. Lett.* **73**, 2920 (1998).
- [42] D. Nečas and P. Klapetek, Gwyddion: An open-source software for SPM data analysis, *Cent. Eur. J. Phys.* **10**, 181 (2012).
- [43] A. Ross, R. Lebrun, O. Gomonay, D. A. Grave, A. Kay, L. Baldrati, S. Becker, A. Qaiumzadeh, C. Ulloa, G. Jakob, F. Kronast, J. Sinova, R. Duine, A. Brataas, A. Rothschild, and M. Kläui, Propagation length of antiferromagnetic magnons governed by domain configurations, *Nano Lett.* **20**, 306 (2019).
- [44] L. Horng, G. Chern, M. Chen, P. Kang, and D. Lee, Magnetic anisotropic properties in Fe_3O_4 and CoFe_2O_4 ferrite epitaxy thin films, *J. Magn. Magn. Mater.* **270**, 389 (2004).
- [45] F. Rigato, J. Geshev, V. Skumryev, and J. Fontcuberta, The magnetization of epitaxial nanometric CoFe_2O_4 (001) layers, *J. Appl. Phys.* **106**, 113924 (2009).
- [46] Y. Zhang, C. Deng, J. Ma, Y. Lin, and C.-W. Nan, Enhancement in magnetoelectric response in CoFe_2O_4 - BaTiO_3 heterostructure, *Appl. Phys. Lett.* **92**, 062911 (2008).
- [47] J. Rodewald, J. Thien, T. Pohlmann, M. Hoppe, F. Timmer, F. Bertram, K. Kuepper, and J. Wollschläger, Formation of ultrathin cobalt ferrite films by interdiffusion of Fe_3O_4 /CoO bilayers, *Phys. Rev. B* **100**, 155418 (2019).
- [48] D. S. Schmool, N. Keller, M. Guyot, R. Krishnan, and M. Tessier, Magnetic and magneto-optic properties of orthoferrite thin films grown by pulsed-laser deposition, *J. Appl. Phys.* **86**, 5712 (1999).
- [49] D. Schmool, N. Keller, M. Guyot, R. Krishnan, and M. Tessier, Evidence of very high coercive fields in orthoferrite phases of PLD grown thin films, *J. Magn. Magn. Mater.* **195**, 291 (1999).
- [50] R. Pauthenet, Spontaneous magnetization of some garnet ferrites and the aluminum substituted garnet ferrites, *J. Appl. Phys.* **29**, 253 (1958).
- [51] Ö. Özdemir, D. J. Dunlop, and B. M. Moskowitz, Changes in remanence, coercivity and domain state at low temperature in magnetite, *Earth Planet. Sci. Lett.* **194**, 343 (2002).
- [52] Ł. Gondek, D. Kaczorowski, and A. Szytuła, Low temperature studies on magnetic properties of Tm_2O_3 , *Solid State Commun.* **150**, 368 (2010).
- [53] A. Barbier, R. Belkhou, P. Ohresser, M. Gautier-Soyer, O. Bezencenet, M. Mulazzi, M.-J. Guittet, and J.-B. Moussy, Electronic and crystalline structure, morphology, and magnetism of nanometric Fe_2O_3 layers deposited on Pt(111) by atomic-oxygen-assisted molecular beam epitaxy, *Phys. Rev. B* **72**, 245423 (2005).
- [54] N. Vlietstra, J. Shan, V. Castel, B. J. van Wees, and J. Ben Youssef, Spin-Hall magnetoresistance in platinum on yttrium iron garnet: Dependence on platinum thickness and in-plane/out-of-plane magnetization, *Phys. Rev. B* **87**, 184421 (2013).
- [55] Y. M. Lu, Y. Choi, C. M. Ortega, X. M. Cheng, J. W. Cai, S. Y. Huang, L. Sun, and C. L. Chien, Pt Magnetic Polarization on $\text{Y}_3\text{Fe}_5\text{O}_{12}$ and Magnetotransport Characteristics, *Phys. Rev. Lett.* **110**, 147207 (2013).
- [56] L. Lang, S. Zhou, and X. Qiu, Surface magnetization thermal fluctuation driven anomalous behaviour of ordinary Hall effect in Pt/YIG, *J. Phys. D: Appl. Phys.* **52**, 085001 (2018).
- [57] L. A. Prelorendjo, C. E. Johnson, M. F. Thomas, and B. M. Wanklyn, A Mossbauer study of spin reorientation in ErFeO_3 , *J. Phys. C: Solid State Phys.* **15**, 3199 (1982).
- [58] G. W. Durbin, C. E. Johnson, and M. F. Thomas, Direct observation of field-induced spin reorientation in YFeO_3 by the Mossbauer effect, *J. Phys. C: Solid State Phys.* **8**, 3051 (1975).
- [59] G. Herrmann, Resonance and high frequency susceptibility in canted antiferromagnetic substances, *J. Phys. Chem. Solids* **24**, 597 (1963).